Delft University of Technology

Practical Investigation of a MIMO radar system capabilities for small drones detection

Yang, Fawei; Xu, Feng; Fioranelli, Francesco; Le Kernec, Julien; Chang, Shaoqiang; Long, Teng

Important note
To cite this publication, please use the final published version (if applicable).
Please check the document version above.

The Institution of
Engineering and Technology WILEY

ORIGINAL RESEARCH PAPER

Practical Investigation of a MIMO radar system capabilities for small drones detection

Fawei Yang[1]　|　Feng Xu[1]　|　Francesco Fioranelli[2]　|　Julien Le Kernec[3]　|　Shaoqiang Chang[1]　|　Teng Long[1]

[1]School of Information and Electronics, Beijing Institute of Technology, Beijing, China

[2]Department of Microelectronics, TU Delft, Delft, The Netherlands

[3]James Watt School of Engineering, University of Glasgow, Glasgow, UK

Correspondence

Shaoqiang Chang, School of Information and Electronics, Beijing Institute of Technology, 100081, Beijing, China.
Email: shaoqiangchang@bit.edu.cn

Abstract

The latest progress of the multiple-input multiple-output (MIMO) radar system developed for small drones detection at Beijing Institute of Technology is presented herein. A low-cost S-band MIMO scanning radar system is designed for the detection of small drones. A practical design optimisation and implementation of a sparse array covering the whole airspace, and a target-based MIMO radar array calibration method to improve the signal-to-noise ratio of the target are proposed. An experiment in the microwave chamber was conducted to verify the designed sparse-array beam-pattern, and measurement campaigns for small drones were performed to test the system performance where the radar achieved detection and tracking of a small DJI-Phantom 4 drone at a range of up to 5 km. Target features, including micro-Doppler and radar cross-section signatures were extracted to assist target classification. The experimental results indicate that the system has promising capability in small drones detection and tracking, despite the challenges of low dwell time on targets due to the scanning nature of the system.

1 | INTRODUCTION

As civilian drone technology continues to mature, small drones are becoming increasingly available to the general public [1]. In recent years, sales of consumer drones have increased significantly due to low prices and user-friendliness [2], and the applications of these unmanned aerial vehicles (UAVs) have become more widespread. The most common uses of UAVs include surveillance and reconnaissance missions, agriculture and environmental monitoring, disaster recovery, as well as private leisure use such as aerial photography and filming [3]. Besides the positive aspects of small UAVs, small drones can also be misused to conduct illegal activities or acts of terror, such as illegal monitoring of restricted areas, smuggling, and collision hazard with buildings and larger aircraft [4], as they can carry small payloads such as cameras, drugs, light firearms, toxic chemicals, or explosives. One of the biggest problems caused by

small drones is disruptions to airport operations. Flights can be grounded when unidentified drones are flying within or close to airport airspace. In 2017, nine illegal drone flights near Chengdu Shuangliu International Airport in southwest China's Sichuan Province caused the cancellation of 43 flights and delay of 142 flights, while another 112 were diverted to alternative airports [5]. Between 19 and 21 December 2018, hundreds of flights were cancelled at Gatwick Airport near London, England, following reports of drone sightings close to the runway. The reports caused major disruption, affecting approximately 140,000 passengers and 1000 flights in a very busy period of the year coinciding with the Christmas holidays [6].

With the rapidly increasing number of security problems caused by non-cooperative drones, there is a strong demand for the development of new detection and tracking technologies for small drones. These are crucial to then enable appropriate pre-emptive measures to stop the offending drones.

There are four main types of drone monitoring equipment, that is, radio frequency (RF) analysers, acoustic sensors (microphones), optical sensors (cameras), and radar [7]. RF analysers can be low cost and passive, but do not always locate and track drones, and cannot detect fully autonomous drones where there is little or no communication with the human operators. Acoustic sensors are medium cost and can provide drone direction, but operate at a very short range and cannot work well in noisy environments (such as airports). Optical sensors can provide visuals of drones, and their potential payload, but suffer from high false alarm rates and poor performance in undesirable lighting conditions or adverse weather conditions such as thick fog. Radars can achieve long-range detection, constant tracking, and highly accurate localisation. They can handle hundreds of targets simultaneously, and track all drones regardless of autonomous flight or weather conditions (day, night, fog, etc.). By analysing the signatures, including their micro-Doppler and other properties, radar systems have the ability to distinguish birds from drones [8]. Thus, radar can be a competitive method to monitor drones and give prospective information about them.

However, small drones detection and tracking can be quite challenging even for radar systems. In general, small drones are typically 'low, slow and small (LSS) targets' which have low flight altitude under 1000 m, slow-flying speed from hovering to 72 km/h, that is 20 m/s [8], and very small radar cross-section (RCS) between 0.01 and 0.1 m^2 [3]. Under these conditions, the signal-to-noise ratio (SNR) of the target is quite low, and the target can be easily overshadowed by stationary background clutter or eliminated by conventional Doppler filtering processes. Furthermore, radar signatures of small drones can be rather similar to other flying targets such as birds, and radar can also detect further moving targets such as larger aircraft, cars, and ships that complicate the situational awareness of the system. This can cause many false alarms and makes it difficult to discriminate small drones from others. The radar tracking problem appears to be also more difficult, as the highly varied motion and high manoeuvrability of small drones make it difficult to make assumptions about the expected motion [1].

Multiple-input multiple-output (MIMO) radar systems have many advantages compared to mechanical scanning systems, or fully filled phased array systems [4, 9]. The wide transmit beam of MIMO radar makes it possible to observe a large area at once and to achieve a long accumulation time, which can improve velocity resolution and mitigate the effects of ground clutter. Meanwhile, the ability to form a rich set of equivalent phase centres and virtual apertures can increase angle resolution as well as achieve moderate system cost compared to phased array radar systems. Considering both the system performance and system cost, the authors decided to design a MIMO radar system for the detection of small drones at the Beijing Institute of Technology (BIT).

The amount of previously available research on radar detection and tracking of small drones when using S-band and experimental data from MIMO or multichannel radar systems is limited. In [10], the author compares staring radar with scanning radar for UAV detection. The paper sets out the advantages of staring radars by introducing the *Alarm* radar,

and it concludes that staring radars give greater confidence in detecting hovering UAVs. In [11], the use of micro-Doppler signatures collected by a multistatic radar called NetRAD is studied to discriminate between hovering and flying small drones while carrying different payloads. Features related to the target RCS, singular value decomposition, and centroid of the micro-Doppler signatures are extracted and the classification performance is above 95% accuracy. In [12], an X-band frequency-modulated continuous waveform (FMCW) radar system called *RAD-DAR* is introduced following the concept of ubiquitous-radar and can achieve small drone detection and tracking at a range up to 3 km. In [13] micro-Doppler spectrograms of different drones and birds using radar systems in millimetre-wave band (W-band, 94 GHz) and K-band are investigated, and in [14] an iterative adaptive approach (IAA) to enhance Doppler resolution is proposed and the micro-Doppler of drones using FMCW radar is examined.

Most of the state-of-art LSS target detection radar systems on the market such as *Robin* and *Aveillant* radar have the ability to filter small drones from birds or other unwanted targets [15, 16]. As for the target classification algorithm, [17] proposes a drone classification method based on convolutional neural network by merging micro-Doppler signature and its frequency domain representation called a cadence-velocity diagram using a Ku-band FMCW radar. The work in [18, 19] focuses instead on a target classification method based on surveillance radar data. The motion models of different targets are established and the model conversion probability is estimated to classify the target type.

In conclusion, most of the systems use FMCW waveforms and staring mode as the coherent accumulation of the target is more efficient compared to the scanning mode. Generally, pulse-Doppler (PD) radar enjoys relatively high transmit power as well as long operating range compared to FMCW radar. Thus the radar system design described herein, which employs PD and MIMO technology in elevation while providing mechanical scanning in azimuth, may combine interesting capabilities in terms of long-range detection, whole airspace coverage, system cost control, as well as multidimensional signal processing.

An expansion of the authors' previous contribution presented at the SEE International Radar Conference in Toulon, France, in September 2019, is presented [20]. That paper presented the initial results of the low-cost S-band MIMO scanning radar, which was developed at the BIT. The radar system employs Doppler division multiple access (DDMA) waveforms [21] to realise orthogonal transmission. A sparse antenna array technique is employed to reduce the system cost and mitigate the influence of the grating lobe. While the conference paper presented only limited experiments in the microwave anechoic chamber and limited basic results of small drone detection and tracking, that analysis is expanded on here. Specifically, more system parameters and theoretical analysis are added to fully characterise the system and its capabilities. For the experimental results, the detection and tracking ability of a DJI Phantom 4 drone with a range of up to 5 km as well as the analysis of range and elevation estimation are illustrated. Moreover, features of the small drone and other targets

including micro-Doppler and RCS signature are extracted to assist target classification. While the study of this radar system yielded some good results, its limitations have to be taken into account, namely the difficulty in detecting hovering drones, the trade-off between detection range and data rate, and relatively low Doppler resolution compared to higher frequency bands. Nevertheless, achieving whole airspace scanning at low cost, 5 km detection range of small drones, and the access to multidimensional signal processing are considered valuable in comparison with state-of-the-art systems and experiments developed in academia.

The radar system is introduced in Section 2, including waveform design, array optimisation, and system configuration and theoretical analysis. The experimental protocol and data analysis are described in Section 3, including anechoic chamber verification, small drone detection and tracking results, and target classification analysis. Finally, further discussions and conclusions are provided in Sections 4 and 5, respectively.

2 | RADAR SYSTEM DESCRIPTION

The radar system used herein was developed at BIT in 2016. It is an S-band coherent pulsed co-located MIMO radar, with six elements. This section provides a description of the system and an explanation of some of the design choices and supporting theoretical assumptions.

2.1 | Waveform design

The DDMA technique is applied in this system to achieve orthogonal transmission and demodulation [22–24]. The DDMA MIMO waveform achieves signal separation by shifting the transmit signals of different transmit antennas to different Doppler frequencies. Compared with other MIMO waveforms such as frequency division multiple access and code division multiple access, DDMA waveform has the advantages of lower range and Doppler side lobes, better system bandwidth utilisation and higher range resolution. The transmitting signal of the DDMA waveform can be described as:

$$u_l(t) = \sum_{m=0}^{M-1} u_p(t - mT_r) e^{j2\pi(f_0 t + \alpha_l mT_r)}, \quad (1)$$

where l and m are the channel and pulse index, respectively. The number of pulses in one coherent processing interval (CPI) is M, and the pulse repetition interval is T_r. The authors chose standard LFM signal as $u_p(t)$ and the carrier frequency as f_0. The instantaneous Doppler frequency of the lth channel was α_l, which can be given as:

$$\alpha_l = -\frac{\Delta f}{2}(L - 1 - 2l). \quad (2)$$

L is the number of channels and Δf is the frequency step size, which can be defined as:

$$\Delta f = f_r / C. \quad (3)$$

f_r is the pulse repetition frequency (PRF) and C is the segment number, which means the number of the sub-PRFs divided from the full Doppler PRF. Figure 1 shows the signal model of the DDMA waveform. By controlling the starting phase of each pulse, the transmitting signal of each channel can be shifted to a different Doppler frequency to transmit orthogonal pulses.

The modulation of the DDMA waveform separates the full Doppler PRF into several segments, which will decrease the unambiguous velocity range of the signal. Also, the phase changing among channels in each pulse generates time-varying transmit weights, which affects the transmit beam-pattern. The physical beam-pattern on each pulse is an angle-shifted version of the transmit beam-pattern, which periodically sweeps across the space as a function of the slow-time pulse m. A sweeping cycle is completed whenever $(\Delta f/f_r)m$ is an integer. That is, the ratio $\Delta f/f_r$, which is also $1/C$, determines the main lobe sweeping rate. Lowering this rate results in a flatter energy coverage, but also gives rise to unused sections of the Doppler domain. These facts should be thoroughly considered in the design of the signal parameters. The authors chose the segment number $C = 16$ to maintain a relatively flat coverage of the transmission power as well as an excellent unambiguous velocity range of ± 39.06 m/s, which can cover the flying speed of most small drones, typically from hovering to approximately ± 20 m/s.
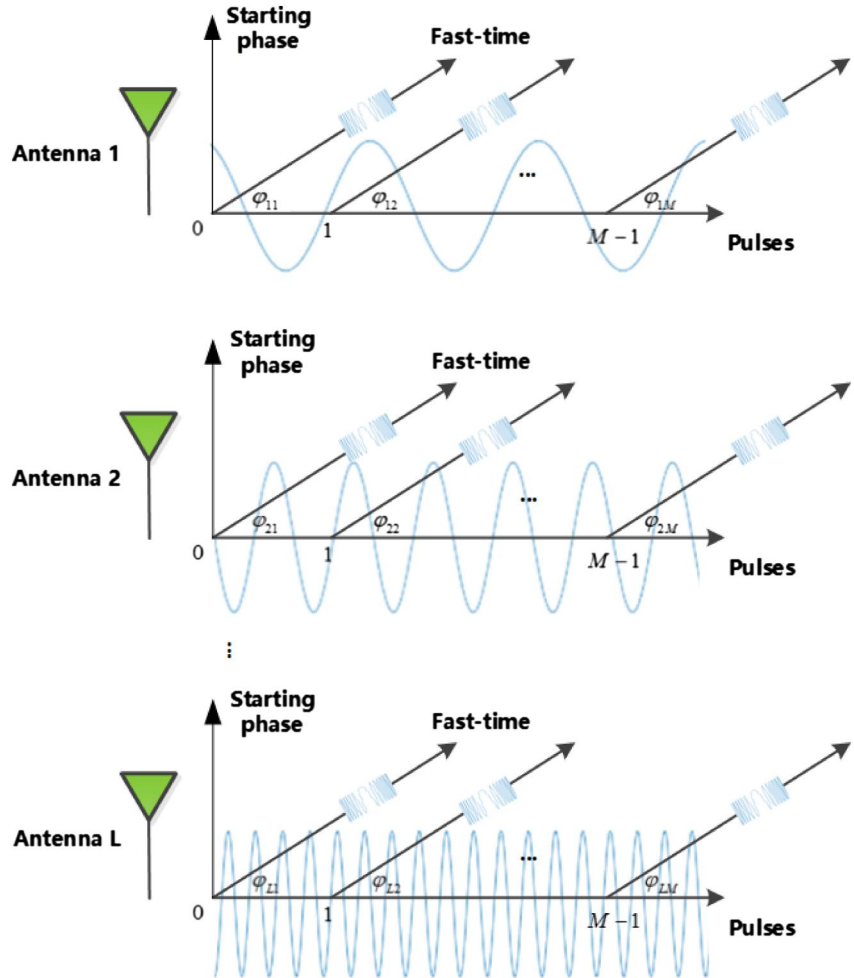
2.2 | Array optimisation

The MIMO radar system is a three-dimensional radar system which utilises mechanical scanning in the horizontal direction and electrical scanning in the vertical direction to obtain the distance, azimuth, and height information of the target. The azimuth beam-pattern of each antenna is a shaped narrow beam, which can achieve horizontal scanning by cooperating with the servo system. The vertical beam-pattern is an approximately omnidirectional wide beam with the main lobe width of 120° to implement MIMO signal transmission and reception. The sparse array technique is utilised to suppress the grating lobe. In this process, a genetic algorithm (GA) is employed to accelerate the search speed of the optimal antenna array positions.

The joint steering vector of MIMO radar is given by

$$\mathbf{B}(\theta) = \mathbf{a}_T(\theta) \otimes \mathbf{a}_R(\theta) \quad (4)$$

where $\mathbf{a}_T(\theta)$ and $\mathbf{a}_R(\theta)$ are the steering vectors of the transmit and receive array with M and N elements, respectively, and $\otimes$ represents the Kronecker product. The two steering vectors can be expressed as:

FIGURE 1 DDMA waveform signal model with L antennas: DDMA waveform adds different starting phase values to different pulses and channels intentionally, so that each channel has a unique Doppler shift. The intrapulse modulation can be the same for every pulse, for example a chirp. DDMA, Doppler division multiple access

$$\mathbf{a}_T(\theta) = \left[e^{-j\frac{2\pi}{\lambda}x_1 \sin\theta}, e^{-j\frac{2\pi}{\lambda}x_2 \sin\theta}, \cdots, e^{-j\frac{2\pi}{\lambda}x_m \sin\theta} \right]^T_{M\times 1}$$

$$\mathbf{a}_R(\theta) = \left[e^{-j\frac{2\pi}{\lambda}y_1 \sin\theta}, e^{-j\frac{2\pi}{\lambda}y_2 \sin\theta}, \cdots, e^{-j\frac{2\pi}{\lambda}y_n \sin\theta} \right]^T_{N\times 1}$$

(5)

where x_m, $m = 1, 2, ... M$, y_n, $n = 1, 2, ..., N$ are the element positions in transmit and receive array, respectively. Thus the joint steering vector $\mathbf{B}(\theta)$ can be expressed as:

$$\mathbf{B}(\theta) = \left[e^{-j\frac{2\pi}{\lambda}(x_1+y_1)\sin\theta}, \cdots, e^{-j\frac{2\pi}{\lambda}(x_1+y_n)\sin\theta}, \cdots, e^{-j\frac{2\pi}{\lambda}(x_m+y_n)\sin\theta} \right]^T_{MN\times 1}$$

(6)

from which the element positions of the virtual array can be expressed as:

$$z_i = x_m + y_n, i = 1, 2, ..., M \times N \qquad (7)$$

Likewise, the synthesised beam-pattern of MIMO radar can be denoted by

$$\begin{aligned} F(\theta) &= \left(\mathbf{w}_T^H \otimes \mathbf{w}_R^H \right) \left(\mathbf{a}_T(\theta) \otimes \mathbf{a}_R(\theta) \right) \\ &= \left(\mathbf{w}_T^H \mathbf{a}_T(\theta) \right) \otimes \left(\mathbf{w}_R^H \mathbf{a}_R(\theta) \right) \\ &= F_T(\theta) \cdot F_R(\theta) \end{aligned}$$

(8)

where $\mathbf{w}_T$ and $\mathbf{w}_R$ represents the weighting vector of the transmit and receive array, respectively. It can be concluded that the MIMO beam-pattern is the product of the transmit and receive beam-pattern. Specifically, for collocated MIMO radar with transmit–receive (T/R) elements, the synthesised beam-pattern can be expressed as:

$$F(\theta) = F_T(\theta) \cdot F_T(\theta) = F_R(\theta) \cdot F_R(\theta) \qquad (9)$$

The virtual array concept of collocated MIMO is shown in Figure 2. Consider a non-uniform sparse MIMO (NUS-MIMO) with the same transmit and receive array, like Figure 2b. The physical aperture of the array is D, and the virtual aperture is $2D$. To simplify the illustration, assume D/λ is an integer, where λ is
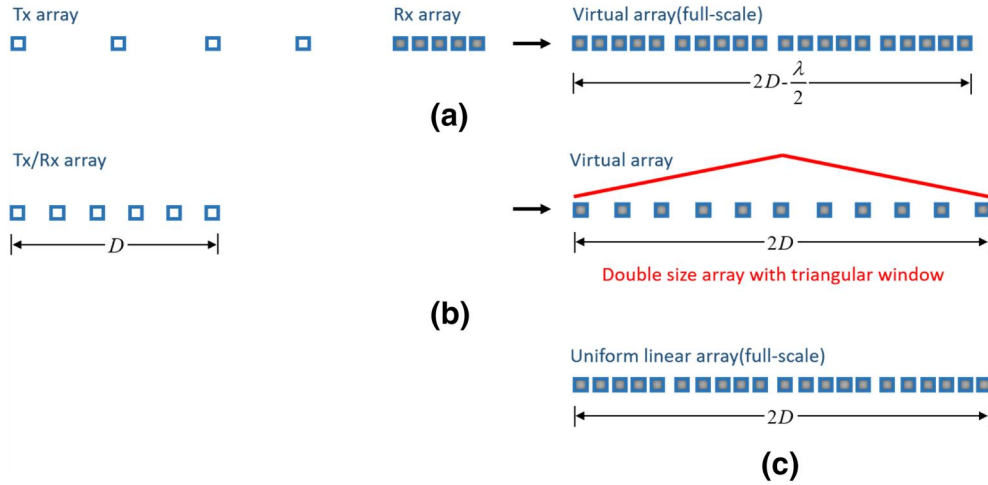
FIGURE 2 The virtual array concept of (a) FS-MIMO, (b) NUS-MIMO, (c) FS-ULA. FS-MIMO, full-scale multiple-input multiple-output; FS-ULA, full-scale uniform linear array; NUS-MIMO, non-uniform sparse multiple-input multiple-output

the wavelength. Let the average interelement space d be λ to obtain a relatively low side lobe level, then the number of elements is $\frac{D}{\lambda}+1$. For a full-scale MIMO (FS-MIMO) with different transmit and receive arrays, like Figure 2a, the number of elements can be expressed as:

$$\left\{ a_i + b_i \,\middle|\, a_ib_i = \frac{4D}{\lambda}, a_i \in \mathbb{N}, b_i \in \mathbb{N}, a_i \le b_i, a_i < a_{i+1} \right\}$$
$$i = 0, 2, \cdots n\text{-}1$$
(10)

It can be seen that the minimum element number of FS-MIMO is $a_n + b_n$. Note that the virtual aperture in this situation is a bit less than NUS-MIMO, which is $2D - \frac{\lambda}{2}$. The number of elements in a full-scale uniform linear array (FS-ULA) for an aperture of $2D$ is $\frac{4D}{\lambda}+1$, as in Figure 2c.

Table 1 lists the array length L in metres together with the minimum element number of FS-ULA, FS-MIMO, and NUS-MIMO with $\lambda = 0.1$ m (S-band). There are four cases with the

array aperture D of 1, 2, 3, and 4 m. For FS-ULA, the interelement spacing is $\frac{\lambda}{2}$. For FS-MIMO with different transmit and receive arrays, the physical length and the elements needed in transmit and receive arrays are displayed, respectively. The beam patterns of FS-ULA and FS-MIMO in case 1 are shown in Figure 3. The 3 dB beam-widths θ_{3dB} of FS-ULA and FS-MIMO in the boresight can be expressed as:

$$\theta_{3dB} \approx \frac{50.8\lambda}{Nd} (°)$$
(11)

which in case 1 are 4.84° and 5.08°, respectively.

It can be seen that both MIMO schemes can save the number of elements, that is the channels of the system, and save cost compared to FS-ULA. When it comes to a cost-sensitive system with a small-scale array, NUS-MIMO can be cost-effective with a smaller antenna size and higher transmit power than FS-MIMO.

TABLE 1 Array length (L) and minimum element number (N) for different architectures (S-band, $\lambda = 0.1$ m)

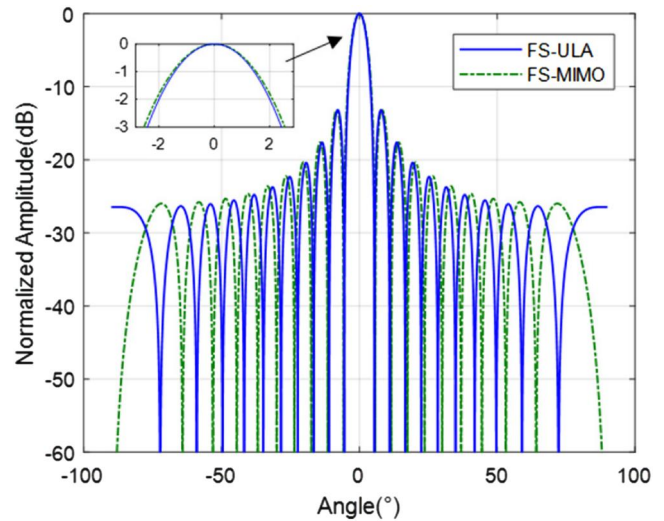|		FS-ULA	FS-MIMO			NUS-MIMO	
		Tx/Rx	Tx	Rx	VA	Tx/Rx	VA
Case 1	$L(m)$	1	0.75	0.2	0.95	0.5	1
	N	21	4	5	20	6	36
Case 2	$L(m)$	2	1.6	0.35	1.95	1	2
	N	41	5	8	40	11	121
Case 3	$L(m)$	3	2.5	0.45	2.95	1.5	3
	N	61	6	10	60	16	256
Case 4	$L(m)$	4	3.5	0.45	3.95	2	4
	N	81	8	10	80	21	441

Abbreviations: FS-MIMO, full-scale multiple-input multiple-output; FS-ULA, full-scale uniform linear array; NUS-MIMO, non-uniform sparse multiple-input multiple-output; Tx/RX, transmit/receive; VA, virtual array.

FIGURE 3 Array beam pattern comparison of FS-ULA and FS-MIMO in case 1: The 3 dB beam-widths are 4.84° and 5.08°, respectively. FS-MIMO, full-scale multiple-input multiple-output; FS-ULA, full-scale uniform linear array

On the contrary, FS-MIMO can significantly reduce the elements needed when the aperture is large. It is also feasible for NUS-MIMO to have a more sparse array with fewer elements, which leads to a trade-off between the system cost and the angle estimation performance.

Due to the physical size of the antenna, the minimum distance between two elements is fixed. This makes it impossible to get a non-grating lobe beam-pattern through array optimisation, because the algorithm cannot choose the element position randomly. Hence, the cost function of the min-max problem is shown as Equation (12) for the GA to search for the suboptimal solution:

$$\min\max F(\theta) \\ s.t. \theta_1 \le |\theta - \theta_0| \le \theta_2 \tag{12}$$

where θ_1 is the first null of the antenna pattern, and θ_2 defines the searching range for the algorithm. Here we let $\theta_2 = 40°$. The main goal of this min-max problem is to reduce the side lobes near the main lobe as much as possible.

The optimised element positions are measured in metre and wavelength and the virtual element positions with collocated element number in brackets are displayed in Table 2. The element positions of the physical T/R and virtual receive array are shown in Figure 4 according to Equation (7), which illustrates that the virtual receive array is twice as large as the physical T/R array with 18 different positions.
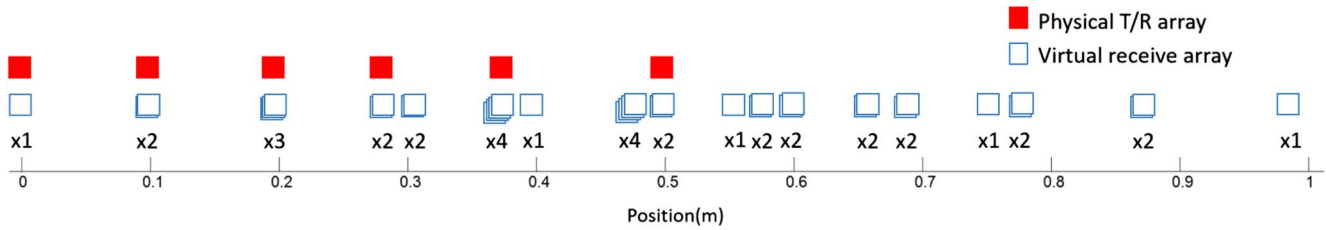
Some positions in the receive array are collocated with more than one virtual element, and the number of the collocated virtual element is indicated below. Figure 5 shows the optimised MIMO beam-pattern together with the physical T/R array beam-pattern (linear phased array) steering to 20° with respect to boresight. It can be seen that there is a grating lobe located at 60° from the main lobe to the left, and the main lobe width of the MIMO beam-pattern (6.2°) is narrower than that of the linear phased array (8.8°), which can improve the angle resolution and estimation accuracy in elevation. Considering the position of the grating lobe together with the ground clutter reflection, the array normal is set to 45° above the horizon level, and the receive beam is usually steered at 20°–40°. Furthermore, the radar system is deployed on a rooftop which is 20 m above the sea level, so that the grating lobe is mostly pointing at the headspace, and we assume that no target or interference is coming from that direction.

2.3 | System configuration and theoretical analysis

The system is configured to use a peak power of 100 W for each channel. There are two different pulse lengths of 1.6 and 10 μs to meet the needs of long-range detection. Other waveform parameters are included in Table 3 and the system performances are summarised in Table 4. In terms of operation mode, the radar system utilises mechanical scanning in azimuth and MIMO digital beam-forming (DBF) in elevation. The system consists of several blocks including antenna array,

TABLE 2 Optimised element positions measured in metres and wavelength, and virtual element positions with collocated element number

	1	2	3	4	5	6	7	8	9	10	11	12	13	14	15	16	17	18
Position (m):																		
Physical elements	0	0.098 (1.08λ)	0.196 (2.16λ)	0.280 (3.08λ)	0.378 (4.16λ)	0.490 (5.39λ)												
Virtual elements	0 (x1)	0.098 (x2)	0.196 (x3)	0.280 (x2)	0.294 (x2)	0.378 (x4)	0.392 (x1)	0.476 (x4)	0.490 (x2)	0.560 (x1)	0.574 (x2)	0.588 (x2)	0.658 (x2)	0.686 (x2)	0.756 (x1)	0.770 (x2)	0.868 (x2)	0.980 (x1)

F I G U R E 4 Element positions of the physical T/R and virtual receive array: The virtual receive array is twice the size of the physical T/R array with 18 different positions. Some positions in the receive array are collocated with more than one virtual element, and the number of the collocated virtual element is indicated below. T/R, transmit–receive
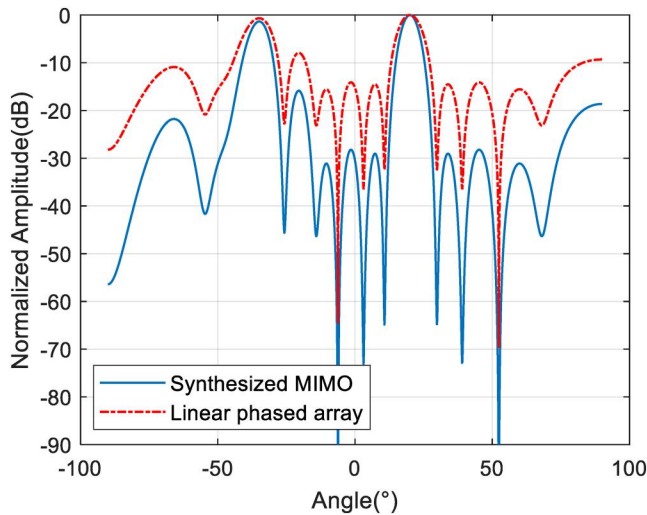
F I G U R E 5 Optimised MIMO beam-pattern together with the physical T/R array beam-pattern (linear phased array) pointing at 20°:.The side lobes near the MIMO beam-pattern main lobe ($\pm 40°$) are under -28 dB, with one strong grating lobe located at 60° away from the main lobe to the left. MIMO, multiple-input multiple-output; T/R, transmit–receive

T A B L E 3 Waveform parameters

Radar frequency	3.3 GHz(S-band)
Bandwidth (B)	40 MHz
Pulse width	1.6/10 μs
Pulse repetition time (PRT)	40 μs
PRF	25 kHz
Number of accumulate pulses (Np)	1024
Segment number	16

Abbreviation: PRF, pulse repetition frequency.

T A B L E 4 System performance

Range resolution	3.75 m
Maximum unambiguous range (Runa)	6 km
Angle resolution after DBF	8°
Doppler resolution	24.41 Hz, 1.22 m/s
Unambiguous velocity range	$-39.06 \sim 39.06$ m/s
Antenna rotation time	4 s

Abbreviation: DBF, digital beam-forming.

RF component, transmit-receive (TR) module, servo system, and signal processing cabinet, as shown in Figure 6. Each of the six antennas can transmit and receive signals under the control of the TR module. Those antennas, which form a linear array in elevation, are designed with combined micro-strip and waveguide technology to achieve a gain of 14 dB. The beam-pattern has a beam-width of 3° in azimuth and 110° in elevation. Figure 7 shows the azimuth and elevation beams. Within the cabinet, there is a graphics processing unit (GPU) to acquire high-speed parallel calculation ability and achieve real-time signal processing. The structure of the entire system is depicted in Figure 8.

Note that MIMO is only formed in elevation and the azimuth scanning is implemented by mechanical scanning with a fixed narrow beam. This design constraint is mainly for the capability of whole airspace coverage at a relatively low cost. Moreover, in elevation, we can still take the advantages of the MIMO radar, resulting in a large virtual array and long accumulation time. It would definitely be more powerful to use planar array MIMO, but also more expensive to cover 360° in azimuth.
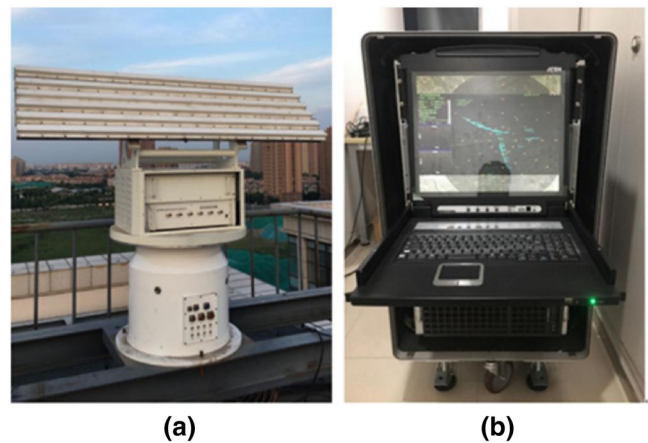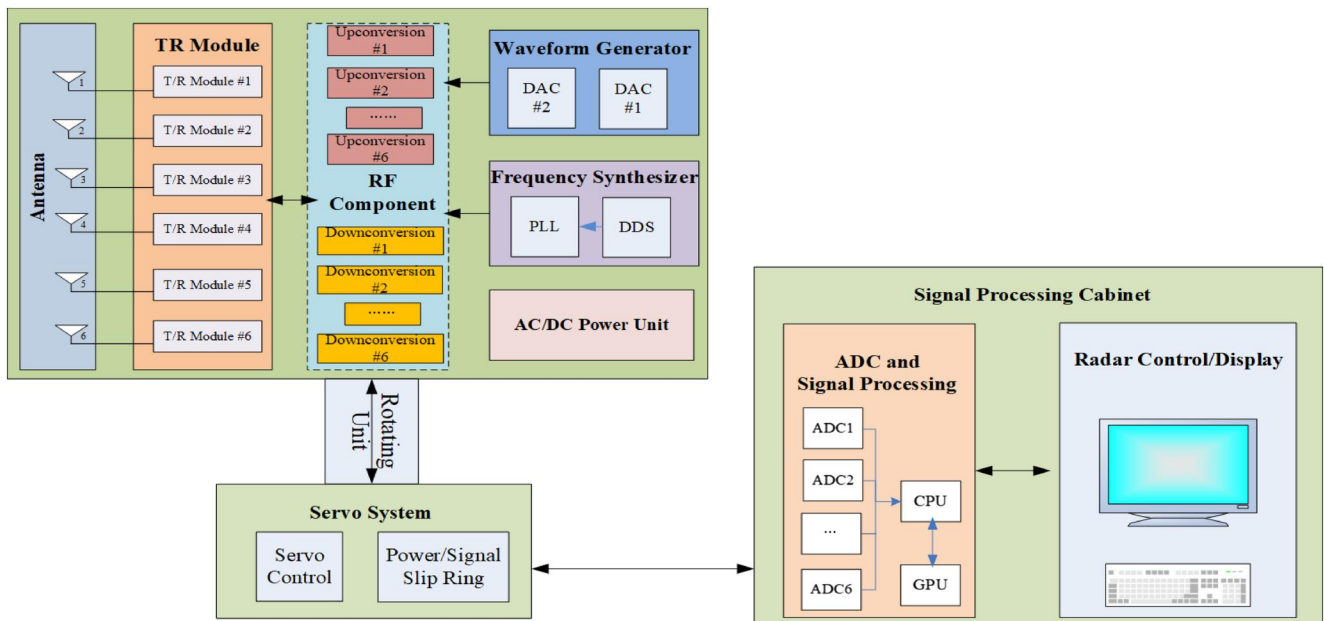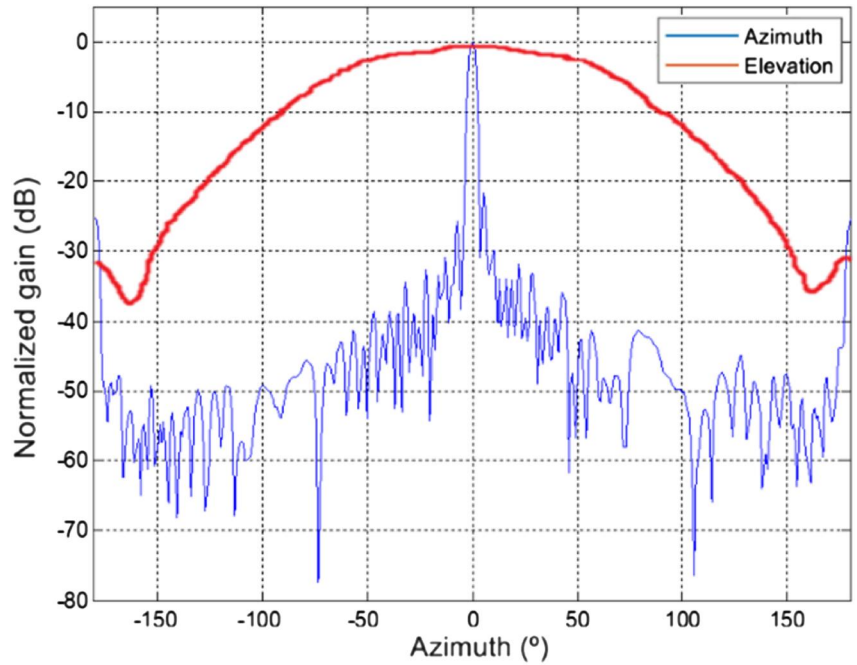

F I G U R E 6 Radar system composition: (a) antenna, RF component and servo, (b) signal processing cabinet. RF, radio frequency

FIGURE 7 Radar antenna radiation pattern: with a beam-width of 3° in azimuth and 110° in elevation

FIGURE 8 Radar system structure: the system mainly consists of an antenna array, transmit/receive module, RF component, waveform generator, frequency synthesiser, servo system, and signal processing cabinet. ADC, analog to digital converter; DAC, digital to analog converter; DDS, direct digital synthesizer; GPU, graphics processing unit; PLL, phase-locked loops; RF, radio frequency; T/R, transmit–receive

According to the radar equation [25], the relationship between the target range R and the SNR is as follows:

$$SNR = \frac{P_t G^2 \lambda^2 \sigma}{(4\pi)^3 R^4 k T_0 BFL_s},\qquad(13)$$

where P_t is the average output power for the TR module, G is the antenna gain, λ is the wavelength, σ is the target RCS, k is the Boltzmann constant, T_0 is the standard temperature, F is

the noise figure of the receiver, and L_s are the system losses. The range-detection probability (P_d) curve is obtained under certain false alarm probability (P_{fa}), which is shown in Figure 9. This curve is calculated with the radar system and waveform parameters, a Swerling I target with $RCS = 0.01\ m^2$ according to [8], and P_{fa} of 10^{-6}, 10^{-7}, and 10^{-8}. This figure predicts the potential capability of the radar to detect a drone within 6 km if false alarm probability is accepted to be at a high-enough value at the target detection stage.
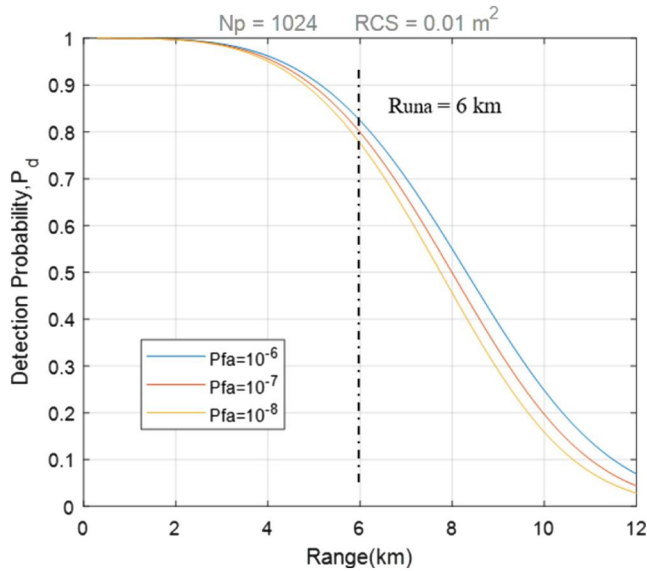
F I G U R E 9 Theoretical range-detection probability curve with different probability of false alarm (P_{fa})

3 | EXPERIMENTS AND DATA ANALYSIS

In this section an experimental analysis of the performance of the proposed radar system is presented, starting with verifications of the antenna array properties in anechoic chamber and then including results from a measurement campaign with a drone (DJI Phantom 4) and several non-drone objects of interest.

3.1 | Verification in an anechoic chamber

An experiment in a microwave anechoic chamber was conducted to test the MIMO beam-pattern. The size of the chamber was $L\,14 \times W\,16 \times H\,15$ m, which was large enough to satisfy the far-field condition in S-band. The servo system was treated as a turntable, and a rack was made to rotate the antenna so that the array was arranged along the horizontal direction. Figure 10 shows the experiment setup in the microwave chamber. The horn antenna transmitted continuous wave (CW) of operating frequency from the signal generator. In the meantime, the radar antenna scanned from −90° to 90° and receives the CW signal. The receive beam-pattern of the six-element linear array was obtained after array calibration and DBF. Furthermore, the synthesised MIMO beam-pattern can be obtained according to Equation (9).

The measured results of the MIMO beam-pattern compare fairly well to the simulation results, which are shown in Figure 11. Note that the element in practice is not identical due to manufacturing constraints and has a wide bell-shaped beam with a main lobe of 110° in elevation, which is shown in Figure 7, the practical side lobes of the synthesised MIMO beam-pattern at large angles are lower than the results in Section 2.2 with identical elements. Thus, in Figure 11, the simulation result with non-
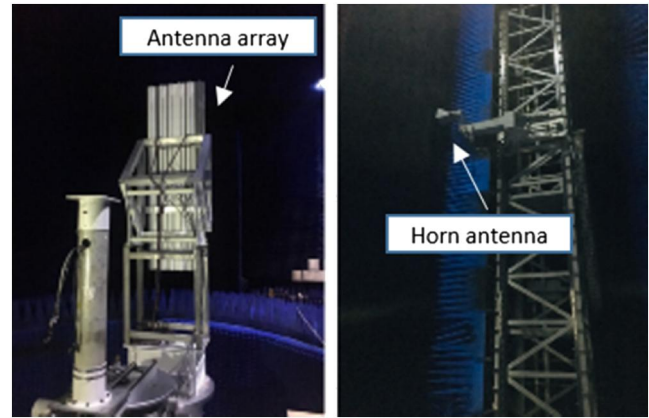

F I G U R E 10 Experimental setup in the microwave chamber

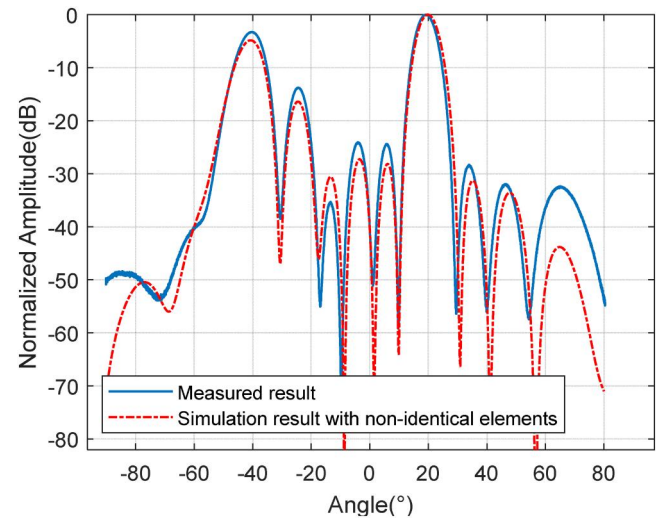**F I G U R E 11** The measurement and simulation results (with non-identical elements) of the synthesised MIMO beam-pattern steering to 20°: main lobe is 6.2° and side lobes within ±40° of the main lobe are below −24 dB. MIMO, multiple-input multiple-output

identical elements has the beam-pattern of the elements added as a weighting vector in order to match a non-identical situation. Generally, the measured result verifies the optimisation method in Section 2.2 with a main lobe of 6.2° and side lobes within ±40° of the main lobe are below −24 dB.

3.2 | Small drone measurement campaigns

A series of detection and tracking experiments on small drones have been conducted to verify the performance of the MIMO radar system. The radar is set on the roof of the building. A DJI Phantom 4 quadcopter was chosen as the target to fly along the radial direction of the radar, with a flying height of 480–500 m and a flying speed of 9–11 m/s. These flight parameters and the linear trajectory ensure that the radar system has good performances in terms of range, speed, and angle estimation errors. The size of the quadcopter is $330 \times 225 \times 405$ mm, and the RCS
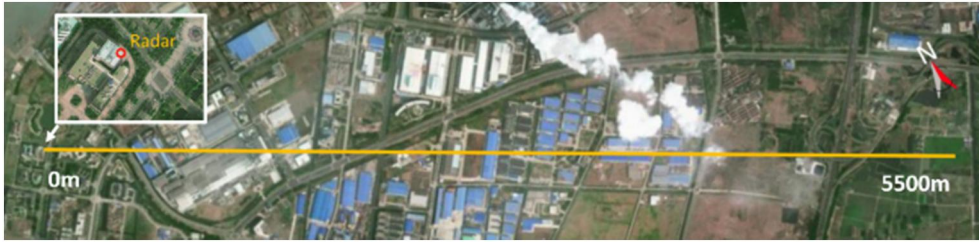
FIGURE 12 Experiment scene: The radar is set on the top of the building and the small drone flies along the radial direction of the radar within 0–5500 m

is between 0.01 and 0.1 m^2 according to the literature [3]. The experiment scene is shown in Figure 12. The radar system is located on the riverside of the Yangtze River, but still in a urban environment, thus there are a large amount of detections and tracks due to the ships on the river and cars on the highway. The small drone's trajectory was selected to avoid tall buildings and ensure good visibility for the radar.

A target-based calibration method for our MIMO radar is proposed to improve the resulting target SNR. Specifically, for the proposed system, the calibration was conducted in elevation. The specific steps of this method are as follows:

(1) In each channel, the signal is digitally down-converted, followed by pulse compression, Doppler processing, and DDMA demodulation to get 36 (6 × 6 MIMO) sets of data in each transmit/receive path.

(2) Detect the target echo of the drone higher than a set threshold, and extract the target's range and Doppler for correction coefficient extraction for the directional of arrival estimation.

(3) Get the amplitude and phase value from the same location in step (2) in each transmit/receive path, that is θ_i and A_i (i = 1, 2,...,36).

(4) Choose the channel that has the most significant amplitude, for example, the kth channel, as the reference to calculate the amplitude and phase error of each channel. The amplitude and phase error can be defined as:

$$\begin{cases} \Delta\theta_i = \theta_k - \theta_i, \\ \Delta A_i = A_k/A_i, \end{cases} \quad i = 1, 2, ...36 \qquad (14)$$

(5) Calculate the theoretical direction of arrival (DOA) of the drone using the range and altitude information, that is α. Then the phase difference φ_i of each channel can be defined as:

$$\varphi_i = \frac{x_i \sin\alpha}{\lambda} 2\pi, \quad i = 1, 2, ...36 \qquad (15)$$

where x_i is the element positions in the virtual array and λ is the operating wavelength of the radar system.

(6) The correction coefficient w_i of the MIMO radar system can be obtained using Equation (16):

$$w_i = \Delta A_i \exp(\Delta\theta_i - \varphi_i), \quad i = 1, 2, ...36 \qquad (16)$$

After calibration, DBF can then be implemented to synthesise received MIMO signals in the direction of interest. The data from each path are combined with the steering vector to obtain the final range-Doppler plane. Figure 13a,b shows the range-Doppler plane of one CPI before and after calibration, from where it can be seen that the SNR of the UAV has been significantly improved after interchannel error calibration.

Table 5 compares the SNR change of different targets before and after calibration. Because of the directivity of the antenna array, the target SNR in the direction of interest is improved while targets in other directions are suppressed. Figure 13c shows the change of the target amplitude of the drone before and after calibration when the steering direction varies from −60° to 60°. This curve can be considered as the MIMO beam-former response to the UAV target. It can be seen that the response is greatly improved after calibration and corresponds well to the simulated and measured MIMO beampattern. Note that the calibration only needs to be performed once after the radar is deployed. Moreover, only one measurement of the target is needed as a reference object. Then all the other targets, as well as the following measurements, can use the same correction coefficients. In addition, the calibration process can be repeated at a certain time interval, such as one month, to keep good angle estimation performance.

Figure 14a–d shows tracking results for the DJI Phantom drone at distances from 1000 to 5000 m, respectively. The root mean-square error is calculated to evaluate the performance of the range measurement capabilities of the system. We compare the radar tracking results with the GPS location shown in the UAV. It can be seen that the detection range with regard to the small drones can be up to 5 km, and the error of the range measurement is lower than 7 m, which is acceptable considering the long distance.

The radar system also implements a mono-pulse technique to estimate the DOA of the target in elevation. Figure 15a,b shows the angle measurement results of two tracks of the drone from 2200 to 3200 m and from 3600 to 4600 m. The mean square error is calculated to evaluate the performance of the elevation angle measurement of the system. From these tracking and measuring results, it can be seen that the MIMO radar system designed here has a good detection and tracking performance for small drones with the detection range of up to 5 km.
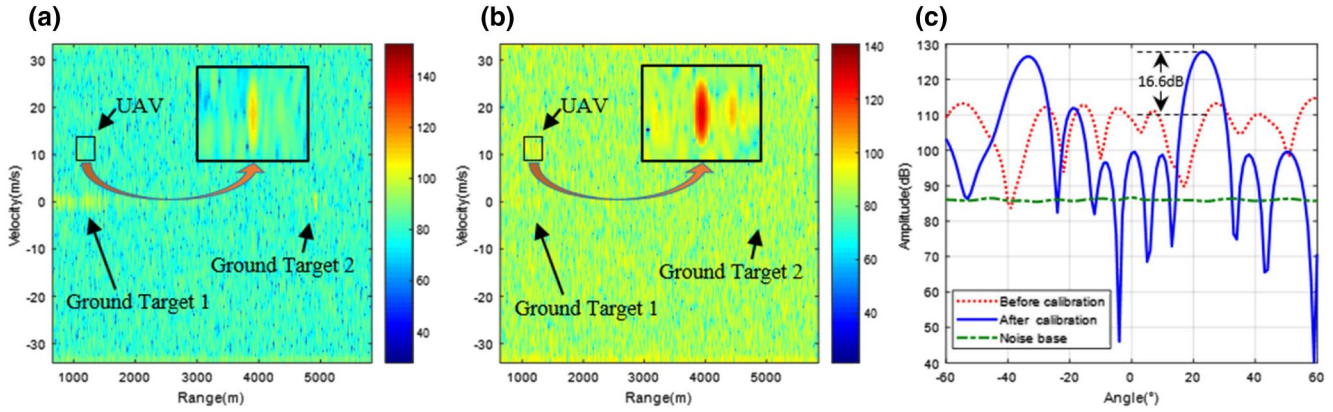
FIGURE 13 Signal processing results after calibration: (a) range–velocity plane before calibration, (b) range–velocity plane after calibration, (c) the MIMO beam-former response to the UAV target before and after calibration (with target SNR improvement of 16.6 dB). MIMO, multiple-input multiple-output; SNR, signal-to-noise ratio; UAV, unmanned aerial vehicle

TABLE 5 Target SNR comparison before and after calibration

	SNR (dB)	
	Before calibration	After calibration
UAV	26.5	43.1
Ground target 1	24.7	15.9
Ground target 2	31.3	8.8

Abbreviations: SNR, signal-to-noise ratio; UAV, unmanned aerial vehicle.

3.3 | Target signatures extraction

As has been stated in Section 3.2, the radar system was deployed in an urban area near the Yangtze River, which led to many detections and tracks belonging to ships and cars. Also, flying birds form misleading tracks for small drone detection, as often noted in the literature. Hence, the study of target signature extraction is of great importance in this context to exclude non-drone targets from detailed analysis. Figures 16 and 17 show the range–velocity plots of different targets at a variety of distances. It can be seen from those figures that all kinds of target appeared to be similar, as a cluster of pixels ('blobs') above the noise level. Further analysis can be performed on these signatures to obtain relevant information and potential features for a target classification process.

3.3.1 | Micro-Doppler signatures

Using micro-Doppler signature is an efficient way to discriminate drones from birds and other targets, and researchers have produced many works on this subject [1, 2, 12–16]. Micro-Doppler is generated by the micro motion of the various components within a target. For small drones, it is generated by the rotation of the propeller blades which leads to rotor blade flashes [13]. Analysing the periodic flashes of the drone or the wing beat frequency of birds provides a way to classify those kinds of targets.

The micro-Doppler analysis described herein applied short-time Fourier transform (STFT) to the range bins where the small drone was present. This STFT used a Hamming window of 43 ms, an overlap of 95% between windows, and a padding of a factor of 4 in the Doppler domain. Figure 18 shows the Doppler profile and time–frequency plot of the drone after STFT. The drone body can be clearly detected within the range of 1178 m and speed of 10.7 m/s, and the bulk velocity is also clearly visible.

However, there are hardly any visible rotator blade flashes on the image. Firstly, the SNR of the blade is too low for the signature to be captured at those long ranges. Furthermore, unlike systems using FMCW or 'staring operation mode' in the literature, this radar operates in track-while-scan mode and the antenna is rotating 360° in azimuth. This design choice enlarges the coverage area but the dwell time is relatively short and the revisiting period is long for the same target. This makes it impossible to obtain a constant and stable data stream for a given target, which degrades the performance of STFT and the possibility of using clear micro-Doppler signatures to aid the target classification process.

3.3.2 | RCS signatures

In this section we focus on how to discriminate small drones from large unwanted targets such as ships using RCS signature. Although the radar system has the ability to measure the target elevation angle using a monopulse approach, this is not always adequate to determine whether the target is flying or on the ground. Especially when the angle resolution is poor, the elevation of a drone flying at a far distance may cover the same range as the ships on the river.

Thus, the target RCS value— σ in Equation (13)—can be derived and taken into account to achieve the classification. The elevation estimation of the two targets is fairly
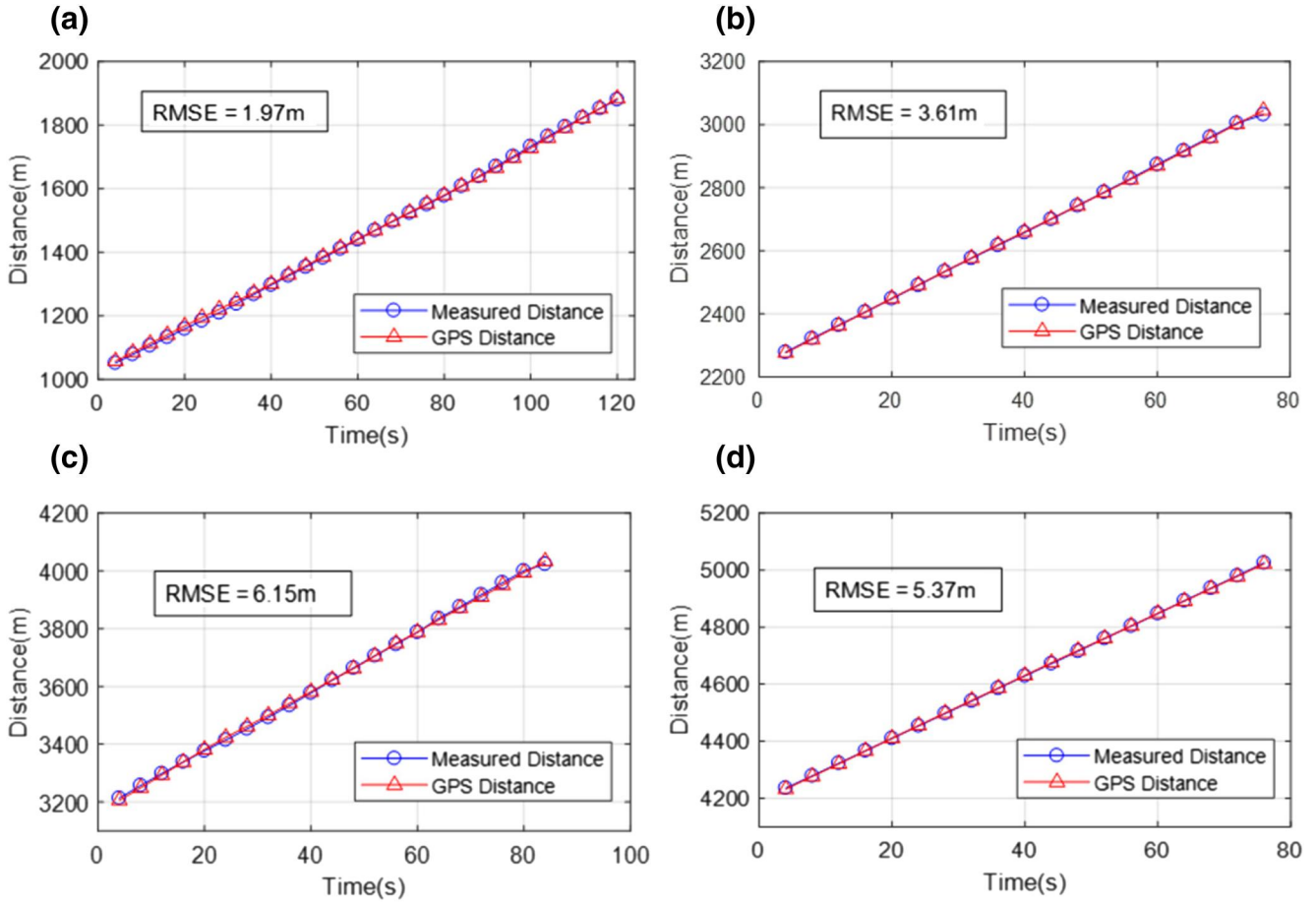
FIGURE 14 MIMO radar system tracking results for the small drone as RMSE of the range for different distances: (a) tracking results from 1000–2000 m, (b) tracking results from 2200–3000 m, (c) tracking results from 3200–4000 m (d) tracking results from 4200–5000 m. MIMO, multiple-input multiple-output; RMSE, root mean-square error
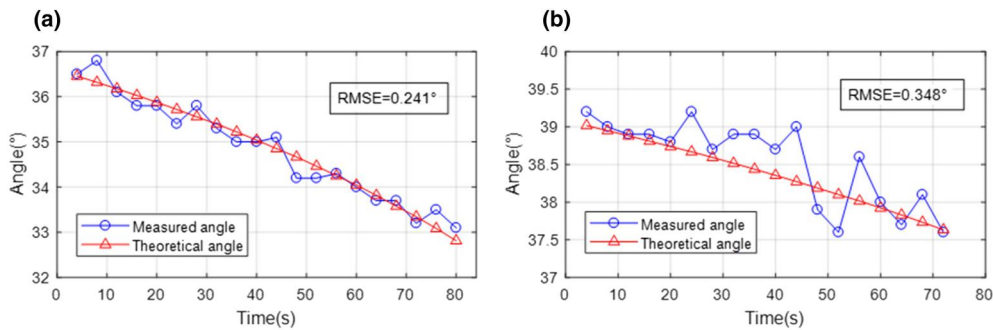
FIGURE 15 Angle measurement results for the small drone as MSE of the elevation angle for different distances of the drone: (a) target from 2200–3200 m, (b) target from 3600–4600 m. MSE, mean square error; RMSE, root mean-square error

comparable, but the SNR extracted from the data shows a significant difference between the two types.

As shown in the feature space plot in Figure 19, the SNR-elevation plot has good interclass separation for ships versus drones. This proves that the RCS signature can be considered as a relevant feature when utilising machine learning-based classification methods such as support vector machine or deep learning-based methods such as neural networks. This could, for example, be used for a quick elimination of targets whose SNR (and RCS) is too large to be a drone. It is also interesting to see a relatively good separation of the samples for the two different models of drones, at least for elevation angle values higher than 5°. This would be an interesting aspect to explore in future work. Note that the features of the ships and drones are very different, especially in RCS; the contribution would be definitely more valuable in distinguishing
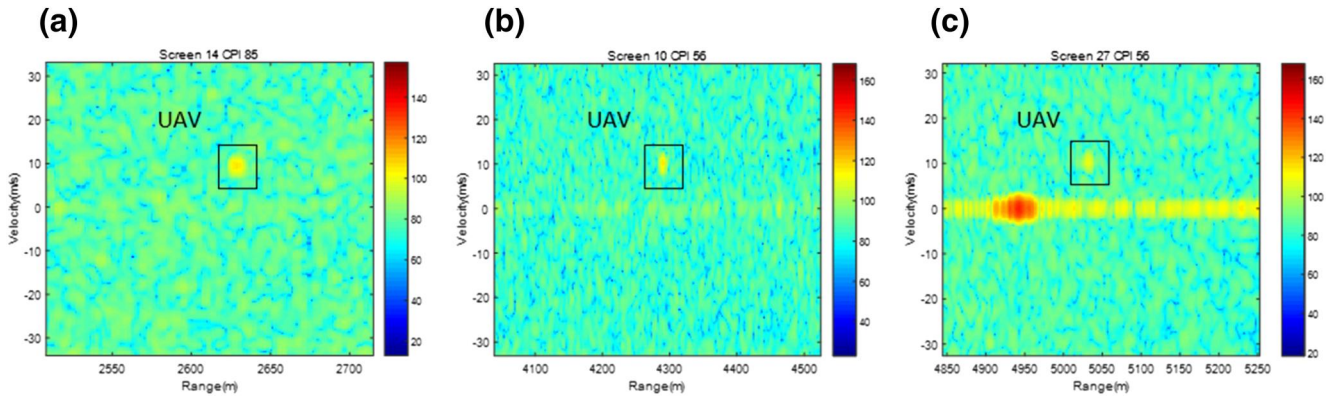
(a) **(b)** **(c)**

FIGURE 16 Range–velocity plane of the drone at different distances: (a) 2630 m, (b) 4290 m, (c) 5034 m. CPI, coherent processing interval; UAV, unmanned aerial vehicle
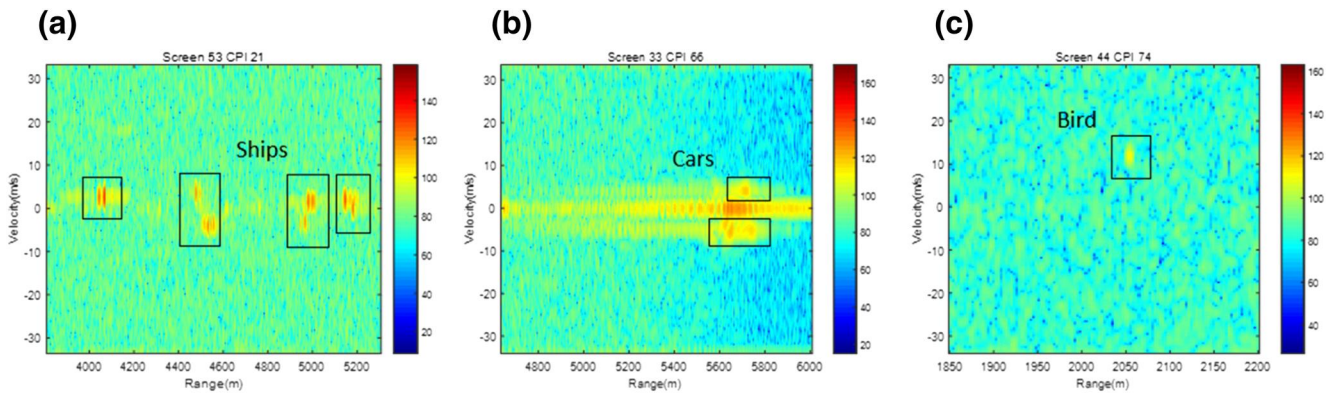
(a) **(b)** **(c)**

FIGURE 17 Range–velocity plane of other different targets: (a) ships on the river, (b) cars on the bridge, (c) birds. CPI, coherent processing interval
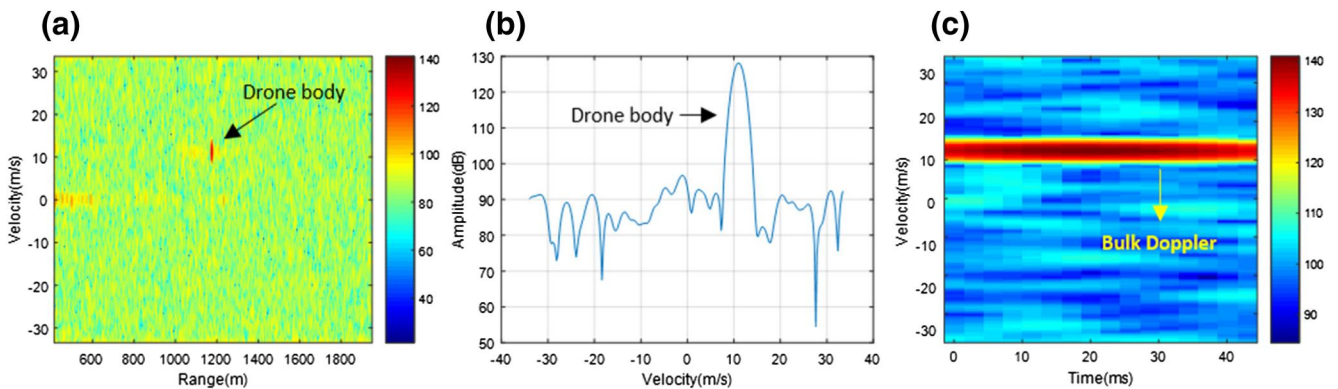
(a) **(b)** **(c)**

FIGURE 18 Radar data domain representation of the drone: (a) range–velocity domain – drone at 1178 m and 10.7 m/s, (b) Doppler profile–peak at 10.7 m/s, (c) velocity–time of the drone after STFT. STFT, short-time Fourier transform

similar targets such as drones and birds. Future work includes micro-Doppler analysis using staring mode, and analysis of the target's micro-Doppler using a different frequency band or polarisation of the radar. Also, the track feature of drones and birds will be investigated as the flying dynamics of the two targets are different.

In addition, other features based on prior knowledge can also be utilised to assist classification. A rough threshold of

the target speed can be set to discriminate drones and some slow-moving ground targets such as ships and human running or cycling. The geographic information can be employed to filter cars on highways. Future works will focus on the combination of those features and improve the performance of the target classification algorithm in a more systematic campaign to construct a necessary database of different target signatures.
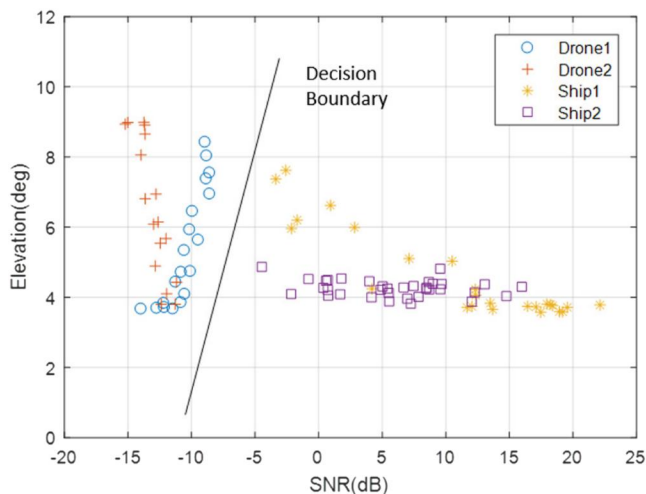
FIGURE 19 SNR-elevation feature plot extracted from the data: better interclass separation can be seen using SNR signature. SNR, signal-to-noise ratio

4 | DISCUSSION

The above sections present some promising results of the proposed radar system, offering whole airspace covering ability and long detection range with acceptable estimation errors of small drones' movements. However, the limitations of the system designed herein should also be considered. Firstly, it is difficult for the radar to detect hovering drones compared to FMCW radar because the scanning scheme constrains the dwell time for the radar illuminating a certain target. Furthermore, the micro-Doppler signature of the target is also difficult to acquire, and the performance of classification methods can be limited in this circumstance due to the lack of such information, often used for automatic target recognition. Potential solutions would be combining the staring mode with the existing scanning mode, that is, keeping the radar beam pointing at the area of interest after some prior information is acquired during the scanning mode. Secondly, for manoeuvring targets, like drones flying in irregular trajectories or birds, there is a trade-off between the detection range and the radar data rate. A higher revisiting time would have better tracking performance for those targets. As for the operating frequency band, higher frequency bands would offer better range and Doppler resolutions and a smaller form factor for the antenna and other hardware, at the cost of higher free space losses and smaller target RCS value.

5 | CONCLUSION

An MIMO radar system for small drones detection and tracking was presented herein. The preliminary results presented in the authors' previous conference paper [20] was expanded upon by designing the suboptimal sparse array and introducing a target-based MIMO radar calibration method. Experiments of array beam-pattern verifying and small drone measurement

campaigns were conducted, and the results showed that the system performed well in detection and tracking of small drones. Furthermore, features of small drones and other targets including micro-Doppler and RCS signature were extracted and preliminarily analysed to assist in target classification.

Future works that should also be considered include target recognition based on machine learning or deep learning methods using combined features, manoeuvring target tracking method, clutter mitigation using wideband radar signal [26], as well as multipath analysis.

ORCID
Fawei Yang 🆔 https://orcid.org/0000-0002-6547-1802
Julien Le Kernec 🆔 https://orcid.org/0000-0003-2124-6803

REFERENCES
1. Hoffmann, F., et al.: Micro-Doppler based detection and tracking of UAVs with multistatic radar. In: Proceedings of the 2016 IEEE Radar Conference, pp. 1–6, Philadelphia (2016)
2. Ritchie, M., et al.: Monostatic and bistatic radar measurements of birds and micro-drone. In: Proceedings of the 2016 IEEE Radar Conference, pp. 1–5, Philadelphia (2016)
3. Ritchie, M., et al.: Micro-drone RCS analysis. In: Proceedings of the 2015 IEEE Radar Conference, pp. 1–5, Johannesburg (2015)
4. Klare, J., Biallawons, O., Cerutti-Maori, D.: UAV detection with MIMO radar. In: Proceedings of the 2017 International Radar Symposium, pp. 1–8, Prague (2017)
5. Gatwick Airport Drone Incident. https://en.wikipedia.org/wiki/Gatwick_Airport_drone_incident. (2021). Accessed 22 February 2020
6. Illegal Drone Flights Raise Concerns. http://www.xinhuanet.com/english/2018-01/21/c_136913048.htm. (2018). Accessed 21 January 2018
7. Countering Drones at Airports. https://www.robinradar.com/countering-drones-at-airports. (2019). Accessed 1 November 2019
8. Patel, J.S., Fioranelli, F., Anderson, D.: Review of radar classification and RCS characterisation techniques for small UAVs or drones. IET Radar, Sonar Navig. 12(9), 911–919 (2018)
9. Zhang, Y., et al.: Colocated MIMO radar waveform design for angular statistical resolution limit in the context of hypothesis testing. Sci. China Inf. Sci. 62(4), 040305 (2019)
10. Harman, S.: A comparison of staring radars with scanning radars for UAV detection: introducing the Alarm™ staring radar. In: Proceedings of the 2015 European Radar Conference, pp. 185–188, Paris (2015)
11. Ritchie, M., et al.: Multistatic micro-Doppler radar feature extraction for classification of unloaded/loaded micro-drones. IET Radar, Sonar Navig. 11(1), 116–124 (2016)
12. Quevedo, Á.D., et al.: Drone detection and radar-cross-section measurements by RAD-DAR. IET Radar, Sonar Navig. 13(9), 1437–1447 (2019)
13. Rahman, S., Robertson, D.A.: Radar micro-Doppler signatures of drones and birds at K-band and W-band. Sci. Rep. 8(1), 1–11 (2018)
14. Sun, H., et al.: Improving the Doppler resolution of ground-based surveillance radar for drone detection. IEEE Trans. Aero. Electron. Syst. 55(6), 3667–3673 (2019)

15. Smart, Affordable Drone Detection Radar. https://www.robinradar.com/elvira-iris-anti-drone-system-brochure. (2020). Accessed 1 Mar 2020

16. Jahangir, M., Baker, C.J., Oswald, G.A.: Doppler characteristics of micro-drones with L-Band multibeam staring radar. In: Proceedings of the 2017 IEEE Radar Conference, pp. 1052–1057, Seattle (2017)

17. Kim, B.K., Kang, H.S., Park, S.O.: Drone classification using convolutional neural networks with merged Doppler images. IEEE Geosci. Rem. Sens. Lett. 14(1), 38–42 (2016)

18. Ghadaki, H., Dizaji, R.: Target track classification for airport surveillance radar (ASR). In: Proceedings of the 2006 IEEE Radar Conference, pp. 1–4, Verona (2006)

19. Chen, W.S., Liu, J., Li, J.: Classification of UAV and bird target in low-altitude airspace with surveillance radar data. Aeronaut. J. 123(1260), 191–211 (2019)

20. Yang, F., et al.: Practical investigation of a MIMO radar system for small drones detection. In: Proceedings of the 2019 IEEE Radar Conference, pp. 1–5, Toulon (2019)

21. Sun, H., Brigui, F., Lesturgie, M.: Analysis and comparison of MIMO radar waveforms. In: Proceedings of the 2014 IEEE Radar Conference, pp. 1–6, Lille (2014)

22. Li, J., Stoica, P.: MIMO Radar Signal Processing. John Wiley & Sons New York (2008)

23. Rabideau, D.J.: MIMO radar waveforms and cancelation ratio. IEEE Trans. Aero. Electron. Syst. 48(2), 1167–1178 (2012)

24. Yang, F., et al.: A DDMA MIMO radar system for low slow and small target detecion. In: Proceedings of the 2018 IET Radar Conference, pp. 1–5, Nanjing (2018)

25. Skolnik, M.: Radar Handbook. McGraw-Hill, New York (2008)

26. Le Chevalier, F., Petrov, N.: Diversity considerations in wideband radar detection of migrating targets in clutter. Sci. China Inf. Sci. 62(4), 040302 (2019)